The Global Nonhydrostatic Model NICAM: numerics and performance of its dynamical core

H. Tomita and M. Satoh

Frontier Research Center for Global Change
3173-25 Showamachi, Kanazawa-ku, Yokohama-city, Kanagawa,236-0001, Japan
htomita@jamstec.go.jp

ABSTRACT

Recently, Frontier Research Center for Global Change (FRCGC) has been developing a new global atmospheric model toward the climate simulation by cloud resolving. The strategy of model development is to use a modified icosahedral grid over the sphere and a new nohydrostatic dynamical scheme suitable to long time integration. In this paper, our recent modeling activity is summarized by focusing on the dynamical core.

1 Introduction

For the modeling of super high-resolution atmospheric/oceanic general circulation, an icosahedral grid has several advantages; the homogeneous and isotropic distribution of gridpoints, the treatment of gridpoint data as two-dimensional structured data in the program code, the easy parallelization on a massively parallel computer with distributed memory, and so on.

The original works of the use of the icosahedral grid in the geophysical problem date back toWilliamson (1968) and Sadourny et al. (1968). These works were followed by (Sadourny, 1969; Williamson, 1969; Cullen, 1974; Cullen and Hall, 1979; Masuda and Ohnishi, 1986). The above icosahedral models suffered from the wave-number 5 problem, which was thought to be a sever drawback of the icosahedral grid and the failures of the predecessors are thought to be due to inappropriate discretization or to relatively lower spatial resolution (Steppeler and Prohl, 1996).

In the 1990s, several research groups have developed icosahedral gridpoint AGCMs using their own new techniques: CSU AGCM at Colorado State University for the climate model (Heikes and Randall, 1995a,b; Ringler et al., 2000) and GME in Deutscher Wetterdienst for the numerical prediction model (Steppeler and Prohl, 1996; Majewski et al., 2002). The Max Planck Institute for Meteorology has also started development of a new dynamical core based on the icosahedral grid configuration (see ICON project[1]). Recently, our research group in Frontier Research Center for Global Change (FRCGC) has been developing a new AGCM, named NICAM (Nonhydrostatic ICosahedral Atmospheric Model). This model is intended to be used for climate study by drastically increasing resolutions on the Earth Simulator(ES)[2]. The ultimate goal of the new model is a global cloud resolving model with 5 km or less in the horizontal directions and 100 m in the vertical direction. In the course of the development of the full AGCM, we have reported the development of a shallow water model based on the icosahedral grid with the improvement of numerical accuracy of the differential operators and homogeneity of the grid system (Tomita et al., 2001, 2002).

For the simulations of such a high horizontal resolution model, the dynamical framework of the atmosphere

[1] http://www.icon.enes.org
[2] http://www.es.jamstec.go.jp/esc/eng/index.html

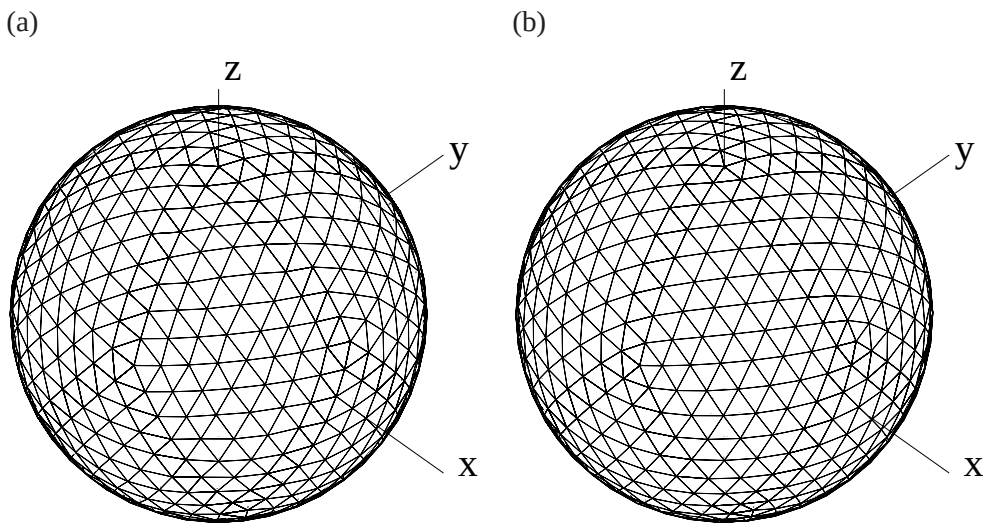

Figure 1: (a) STD-grid with glevel-3. (b) SPR-GC-grid with glevel-3.

should be switched from the usually used hydrostatic primitive equations to the nonhydrostatic ones. Although there exist many established regional nonhydrostatic models, most of them are based on numerical schemes that do not guarantee the conservation of mass and total energy. Since we intend to perform long time simulations for climate study, the conservation of mass and total energy is particularly required. Satoh (2002, 2003) developed a nonhydrostatic regional model with a new scheme that completely satisfies the conservation of these quantities and showed its numerical results. We implement this nonhydrostatic scheme to a global model based on the icosahedral grid configuration.

In this paper, we introduce our new modeling of nonhydrostatic global model and show its physical and computational performances. Basically, this paper is a brief summary of our recent modeling activity (Tomita et al., 2001, 2002; Satoh, 2002, 2003; Tomita et al., 2004; Tomita and Satoh, 2004).

2 Horizontal discretization

2.1 Grid refinement and discretization of differential operator

The refinement of grid is done by the general recursive technique which is similar to that ofStuhne and Peltier (1996, 1999). In this paper, the grid resolution obtained by l-th dividing operation is called "glevel-l". Hereafter, the grid thus determined will be called the *STD*-grid (Fig. 1(a)). All the variables are defined at the vertices of triangular grid elements. This arrangement is something like the Arakawa-A type grid. The control volume is defined as the polygon constructed by connecting the gravitational centers of neighboring triangular grid elements. The shape of control volume is hexagon except that it is pentagon at only twelve points inherited from the original icosahedron.

We employ the finite volume method for the discretization of differential operators. For example, the divergence operator is discretized as follows. Figure 2(a) shows the schematic figure of horizontal control volume. If a set of vectors $\mathbf{u}$ is given at all the vertices of triangles P_i, vectors $\mathbf{u}$ at the vertices of control volume Q_i are interpolated as

$$\mathbf{u}(Q_i) \simeq \frac{\alpha\mathbf{u}(P_0) + \beta\mathbf{u}(P_i) + \gamma\mathbf{u}(P_{1+mod(i,6)})}{\alpha+\beta+\gamma}, \tag{1}$$

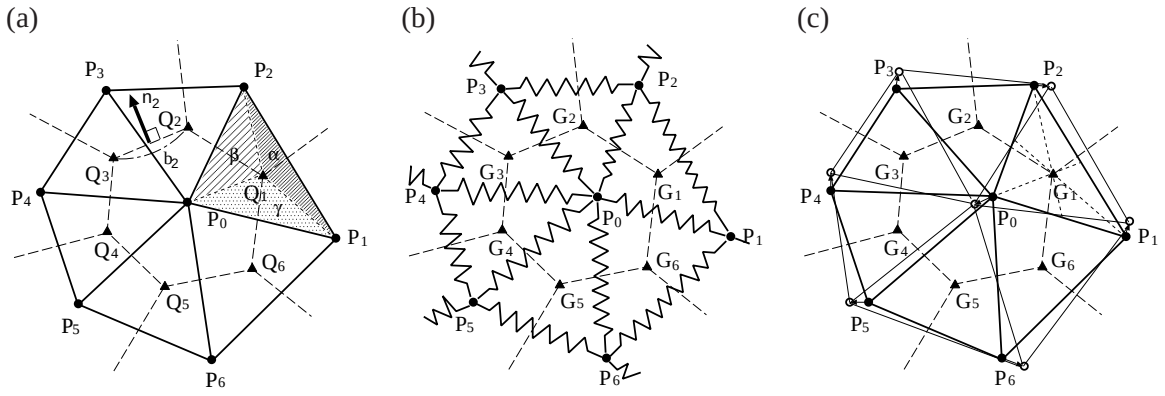

Figure 2: (a) Schematic figure of control volume. (b) Modification by the spring dynamics. (c) Modification by the gravitational center reallocation.

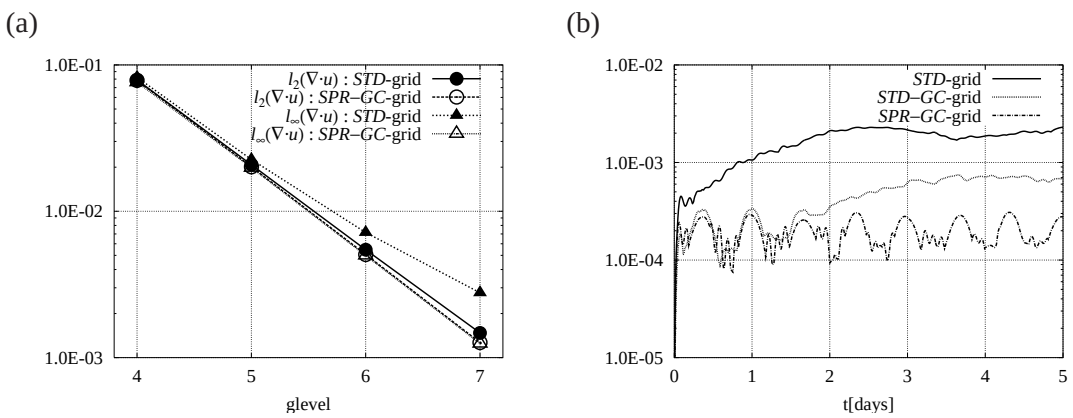

Figure 3: (a) Comparison of convergence properties between STD-grid and SPR-GC-grid for the divergence operator. (b) Comparison of l_{inf} error for Test Case 2.

where α, β, and γ are the areas of $Q_iP_iP_{1+mod(i,6)}$, $Q_iP_{1+mod(i,6)}P_0$, and $Q_iP_0P_i$, respectively. The number 6 is replaced with 5 at the pentagonal control volumes. The divergence is calculated from the Gauss theorem as

$$\nabla\cdot\mathbf{u}(P_0) \simeq \frac{1}{a(P_0)}\sum_{i=1}^{6} b_i \frac{\mathbf{u}(Q_i)+\mathbf{u}(Q_{1+mod(i,6)})}{2}\cdot\mathbf{n}_i, \tag{2}$$

where b_i and $\mathbf{n}_i$ denote the geodesic arc length of $Q_iQ_{1+mod(i,6)}$ and the outward unit vector normal to this arc at the midpoint of $Q_iQ_{1+mod(i,6)}$. $a(P_0)$ is the area of control volume at the point P_0.

2.2 Modified icosahedral grid

The combination of the *STD*-grid and the discretization like Eq.(2) has some problems on the numerical accuracy and stability. We propose a modification method of icosahedral grid in order to reduce the systematic grid noise and to improve the accuracy of operators(Tomita et al., 2001). There are two steps in this method. In the first step, we consider an application of spring dynamics as follows. Grid points are connected by ap-

propriate springs (Fig.2(b)). Starting from an appropriate initial condition, the equations of spring dynamics are numerically solved until the dynamical system calms down. We found that this modification dramatically reduce the grid-noise in the numerical integration of equations.

In the second step, the locations of gridpoints are moved to the gravitational centers of control volumes as in Fig.2(c). We found that this modification guarantees the 2nd order accuracy of differential operator everywhere. We call thus modified grid system the *SPR-GC*-grid. Figure 3(a) indicates an example of improvement of accuracy by the grid modifications for the divergence operator, where **u** denotes the vector field which has appropriate wave-like distribution both in the longitudinal and latitudinal directions, l_2 norm represents the global error, while l_∞ norm represents the maximum of the local error. As shown in Fig.3(a), the modifications provide the ideal second order accuracy both in the global sense and in the local sense.

We can show that the grid modification is useful by conducting the standard test case 2 of shallow water model (Williamson et al., 1992). Figure 3(b) shows the time histories of l_∞ norm of height field for the *STD*-grid, the *STD-GC*-grid[3], and the *SPR-GC*-grid. l_∞ norm of the *STD*-grid is larger than the others from the initial stage and it becomes much larger as time goes on. This is because the discretized operators for the *STD*-grid is less accurate than that in the other grids. *STD-GC*-grid has better accuracy, but l_∞ norm of this grid becomes larger after that. The reason why the result of the *STD-GC*-grid becomes worse can be explained as follows; although the discretized operator of the *STD-GC*-grid is more accurate than that of the *STD*-grid, it include the systematic errors due to non-smoothness of grid. This leads to a small grid noise occurring initially is amplified in time and finally the whole field are contaminated by the noise. Although there is a small error also in the *SPR-GC*-grid, it is not amplified owing to smoothness of grid. Consequently, the small error of the *SPR-GC*-grid can be kept during 5 days.

3 Nonhydrostatic framework

3.1 Governing equations

The governing equations employed in the 3D model are based on the Euler's equations without any approximation. In the traditional atmospheric models, the shallow atmosphere approximation has been used conventionally. One may point out, however, that this approximation leads to inconsistency for conservation of the absolute angular momentum unless several metric terms and the vertical Coriolis term are neglected (Phillips, 1966; Kasahara, 1974; Staniforth and Wood, 2003); if the equation of absolute angular momentum is constructed from the set of momentum equations, the global integration of the absolute angular momentum is not guaranteed for the sake of this approximation. We introduce a "deep" factor :

$$\gamma \equiv r/a, \tag{3}$$

where r and a denote the distance form the center of earth and the earth radius at the sea level, respectively.

For the treatment of topography, we employ the terrain-following coordinate with the metrics as

$$\xi = \frac{z_T(z - z_s)}{z_T - z_s}, \quad G^{1/2} \equiv \left(\frac{\partial z}{\partial \xi}\right)_h, \quad \mathbf{G^z} \equiv \nabla_{h0}\xi = -\frac{\tilde{\nabla}_{h0} z}{G^{1/2}}, \tag{4}$$

where z_T and z_s are the top of the model domain and the surface height and $(\partial/\partial\xi)_h$ denotes the derivative along the vertical direction and $\tilde{\nabla}_{h0}$ denotes the spherical gradient operator along a constant ξ plane at the sea level ($r = a$).

[3] where *STD-GC*-grid means the grid only with gravitational center reallocation

Since $G^{1/2}\gamma^2$ is the factor of volume against the surface, we treat the prognostic variable multiplied by this factor, i.e., the perturbation density $R = (\rho - \rho_{ref})G^{1/2}\gamma^2$ (subscript ref stands for the hydrostatic reference state), the horizontal momentum $\mathbf{V}_h = \rho G^{1/2}\gamma^2\mathbf{v}_h$, the vertical momentum $W = \rho G^{1/2}\gamma^2 w$, and the internal energy $E = \rho G^{1/2}\gamma^2 e$. The governing equations for these quantities can be written as

$$\frac{\partial R}{\partial t} + \tilde{\nabla}_{h0}\cdot\frac{\mathbf{V}_h}{\gamma} + \frac{\partial}{\partial \xi}\left(\frac{\mathbf{V}_h}{\gamma}\cdot\mathbf{G}^{\mathbf{z}} + \frac{W}{G^{1/2}}\right) = 0, \tag{5}$$

$$\frac{\partial \mathbf{V}_h}{\partial t} + \tilde{\nabla}_h\frac{P}{\gamma} + \frac{\partial}{\partial \xi}\left(\mathbf{G}^{\mathbf{z}}\frac{P}{\gamma}\right) = -\tilde{\mathbf{A}}_h - \tilde{\mathbf{C}}_h, \tag{6}$$

$$\frac{\partial W}{\partial t} + \gamma^2\frac{\partial}{\partial \xi}\left(\frac{P}{G^{1/2}\gamma^2}\right) + Rg = \left(-\tilde{A}_z - \tilde{C}_z\right), \tag{7}$$

$$\begin{aligned}&\frac{\partial E}{\partial t} + \tilde{\nabla}_{h0}\cdot\left(h\frac{\mathbf{V}_h}{\gamma}\right) + \frac{\partial}{\partial \xi}\left[h\left(\frac{\mathbf{V}_h}{\gamma}\cdot\mathbf{G}^{\mathbf{z}} + \frac{W}{G^{1/2}}\right)\right]\\ &- \left[\mathbf{v}_h\cdot\left(\tilde{\nabla}_{h0}\frac{P}{\gamma} + \frac{\partial}{\partial \xi}\left(\mathbf{G}^{\mathbf{z}}\frac{P}{\gamma}\right)\right) + w\left(\gamma^2\frac{\partial}{\partial \xi}\left(\frac{P}{G^{1/2}\gamma^2}\right) + Rg\right)\right] + Wg = \tilde{Q}_{heat},\end{aligned} \tag{8}$$

where $P = (p - p_{ref})G^{1/2}\gamma^2$ is the perturbation pressure, h enthalpy, g the gravitational acceleration, and$\tilde{Q}_{heat}$ the heating rate.

$\tilde{\mathbf{A}}(= \tilde{\mathbf{A}}_h + \tilde{A}_z\mathbf{k})$ and $\tilde{\mathbf{C}}(= \tilde{\mathbf{C}}_h + \tilde{C}_z\mathbf{k})$ are momentum advection term and Coriolis term, respectively Here, we introduce an orthogonal basis $\{\mathbf{e}_1, \mathbf{e}_2, \mathbf{e}_3\}$, which is independent of space with $\mathbf{e}_3$ being in the same direction as the angular velocity of the earth $(0, 0, \Omega)$. We define v_1, v_2, and v_3 as the components of the three-dimensional velocity $\mathbf{v}$ with regard to the basis $\mathbf{e}_1$, $\mathbf{e}_2$, and $\mathbf{e}_3$, respectively. $\tilde{\mathbf{A}}$ and $\tilde{\mathbf{C}}$ can be expressed as

$$\tilde{\mathbf{A}} \equiv \sum_{i=1}^{3}\left[\tilde{\nabla}_{h0}\cdot\left(v_i\frac{\mathbf{V}_h}{\gamma}\right) + \frac{\partial}{\partial \xi}\left[v_i\left(\frac{\mathbf{V}_h}{\gamma}\cdot\mathbf{G}^{\mathbf{z}} + \frac{W}{G^{1/2}}\right)\right]\right]\mathbf{e}_i, \tag{9}$$

$$\tilde{\mathbf{C}} \equiv 2\Omega\rho G^{1/2}\gamma^2\left(-v_2\mathbf{e}_1 + v_1\mathbf{e}_2\right). \tag{10}$$

3.2 Numerical method

Since the set of governing equations we solve is an elastic system, it may contain all of the waves realized in the actual atmosphere. The acoustic waves and the high-frequency gravity waves together with the Lamb waves are contained as the fast modes. If a fully explicit method is employed to solve Eqs.(5)-(8), the time interval is severely restricted due to the vertical propagation of the acoustic waves. On the other hand, if an implicit method is employed for both in the horizontal and vertical directions, one has to solve a three-dimensional Helmholtz equation for pressure or vertical momentum. It is thought that a computational cost is high in solving a multi-dimensional Helmholtz equation especially for high resolution simulations. In order to avoid solving a multi-dimensional Helmholtz equation, we decided to integrate the equations implicitly in the vertical direction and explicitly in the horizontal directions. This method is called the Horizontally Explicit and Vertically Implicit scheme (HEVI). Satoh (2002, 2003) proposed a new nonhydrostatic scheme in the context of the HEVI scheme. In order to use it for climate simulations, he formulated the scheme by taking the conservation of mass and total energy into consideration. We extend this scheme to the global domain using the icosahedral grid.

In Eqs.(5)-(8), the left-hand side terms are associated with fast propagating waves in space, while the right-hand side terms are related to relatively slow motions. We refer the former to fast mode terms and the latter to slow mode terms in this paper.

We integrate the prognostic variables with the time-splitting method, namely, the fast mode terms are evaluated at every small time step $\Delta\tau$, while the slow mode terms are evaluated at larger time step Δt. For the small time

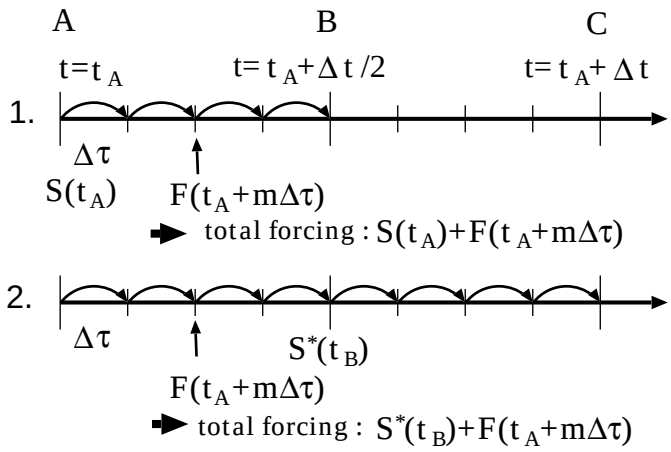

Figure 4: Schematic diagram of temporal integration.

step integration we use the forward-backward scheme based on the HEVI scheme, while for the large time step integration we use the 2nd-order Runge-Kutta scheme. This integration strategy is similar to that of the WRF (Weather Research and Forecasting) model developed in NCAR (Wicker and Skamarock, 1998, 2002). Figure 4 schematically shows the time integration procedure. Let Eqs.(5)-(8) be described schematically as

$$\frac{\partial \Psi}{\partial t} - F = S, \tag{11}$$

where Ψ, F, and S represent the prognostic variable, the fast mode term, and the slow mode term, respectively. If Ψ at $t = t_A$ is known, we can evaluate the slow mode tendency $S(t_A)$. The variable is integrated from t_A to t_B by using $S(t_A) + F(t_A + m\Delta\tau)$ as the forcing at $t = t_A + m\Delta\tau$ with the fast mode tendency $F(t_A + m\Delta\tau)$ being updated at every small step, where m represents the index of small time step. Thus, the temporary value of the prognostic variable Ψ^* at t_B can be obtained. Using this value, we can evaluate the slow mode tendency $S^*(t_B)$. Returning to $t = t_A$, the variable is integrated from t_A to t_C by using $S^*(t_B) + F(t_A + m\Delta\tau)$.

The fast mode is integrated by the forward-backward method with a small time interval. The small time step integration contains the following three steps:

1. Eq.(6) is temporally evolved to update $\mathbf{V}_h$.
2. The one-dimensional Helmholtz equation for W constructed by coupling Eqs.(5), (7), and (8) is solved by a tri-diagonal matrix inversion to obtain R, W, and E.
3. The internal energy is corrected so as to conserve the total energy. Actually, the total energy equation with flux form is solved in this step.

The detail formulation of this method can be described in Satoh (2002); Tomita and Satoh (2004).

4 Test of dynamical core and computational performance

4.1 Held-Suarez Test Case

We have already performed a lot of preliminary tests for the dynamical core of NICAM (Tomita and Satoh, 2004). In this paper, we just show the result of Held and Suarez (1994) Test Case (HSTC), comparing with

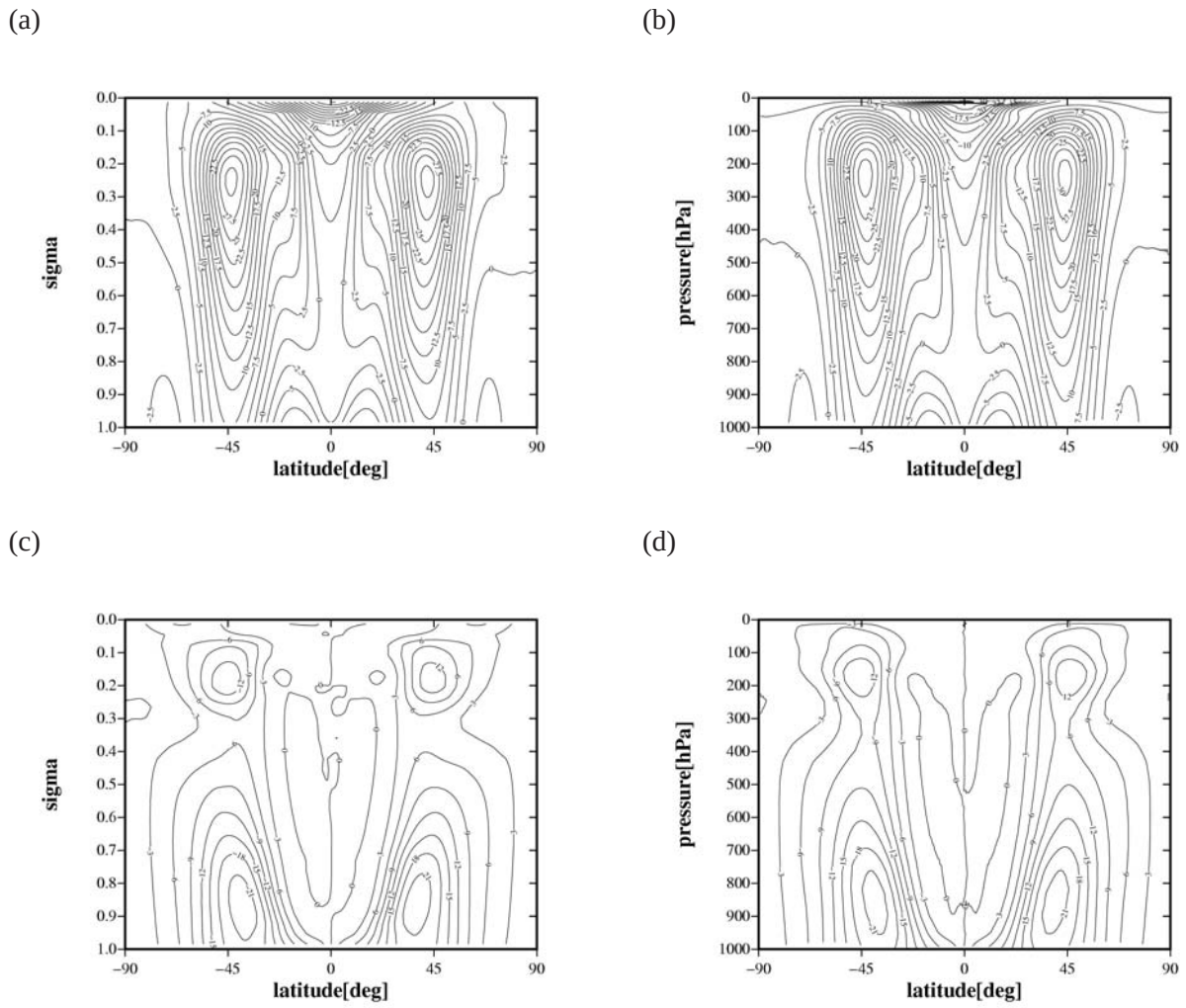

Figure 5: (a) Zonal mean of zonal wind (AFES) (b) Zonal mean of zonal wind (NICAM) (c) Zonal mean of eddy heat transfer (AFES) (d) Zonal mean of eddy heat transfer (NICAM)

a spectral transform model. For this comparison, we use AFES (AGCM For Earth Simulator, Shingu et al. (2002))[4] as a spectral transform model.

Figure 5 gives the comparison of AFES (T159) and NICAM (glevel-6) for climatology of zonal wind and eddy heat transfer. In both of models, the number of vertical levels is 32 and we use the 4-th order horizontal diffusion, coefficient of which is given as 1.25×10^{15} m^4/s. As shown in Fig.5, the defference between two models is not significant; the intensity and location of westerly jet and peak of eddy heat transfer.

[4] Substantially, the dynamical and physical processes in AFES are based on CCSR/NIES AGCM, which has been developed by Center of Climate System Research in University of Tokyo and National Institute Environmental Studies.

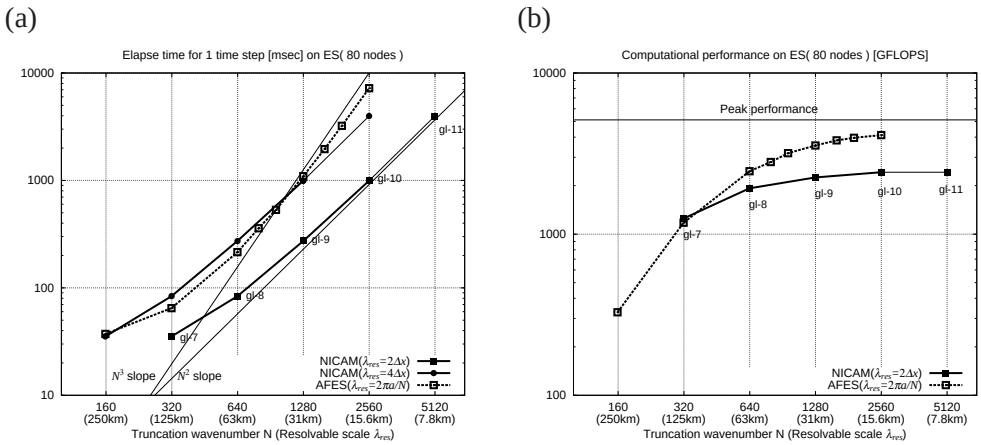

Figure 6: (a) Comparison of elapse time for 1 time step between AFES and NICAM. λ_{res} stands for the resolvable scale on the equator. (b) Comparison of computational performance between NICAM and AFES.

4.2 Computational performance

For estimation of computational performance, the horizontal resolution increases from T159 to T2559 for AFES and from glevel-7 to glevel-10 for NICAM. All of measurements were performed by using 80 nodes of the ES.

The term "resolution" is sometimes ambiguously defined in many literatures, especially, for the spectral transform method. The grid interval at the equator estimated by $2\pi a/(3N+1)$ is often used as the resolution for spectral models, where N is the truncation wavenumber. As pointed out by R.Laprise (1992), this estimation is very optimistic because the waves with wavelength less than $2\pi a/N$ is actually cut off. R.Laprise (1992) suggested the possibility that the resolution in the spectral model becomes worser than $2\pi a/N$ from the viewpoints of the degree of freedom and the Fourier mode analysis. On this consideration, the resolvable scale for the spectral model should be defined at least as $\lambda_{res} = 2\pi a/N$. On the other hand, the resolvable scale in the gridpoint method is easily defined as two-grid scale from the sampling theory. By this criterion, the resolution of glevel-7, 8, 9, and 10 is about 120 km, 60 km, 30km, and 15km, respectively.

The line with black rectangles in Fig.6(a) indicates the elapse times of one time step of NICAM. The line for NICAM in Fig.6(a) is close to N^2 slope in higher resolutions. This tendency is reasonable because the flops value is almost saturated at glevel-10 as shown in Fig.6(b). The value at glevel-11 (3.5 km grid interval) is easily guessed from the tendency between glevel-9 and 10.

On the other hand, the line of AFES in Fig.6 (the line with white rectangles) is close to N^3 slope in higher resolutions than T1279. This tendency means that the calculation amount of Legendre transformation becomes dominant over the other processes; the flops value becomes saturated as shown in Fig6(b).

The available time interval without numerical instabilities is also an important factor. By performing 1000 days integration on the condition of HSTC, we investigated the maximum time intervals Δt_{max} as increasing Δt by 50 sec for T159 (AFES) and for glevel-7 (NICAM). Table 1(a) and (b) show the results of Δt_{max} at these resolutions (bold letters). We can estimate the maximum time intervals in higher resolutions for NICAM, because this model employ a quasi-uniform grid; if the resolution becomes double, the maximum interval becomes half. For the spectral model AFES, the criterion for the maximum time interval is not clear but it is empirically known that the maximum time interval is in inverse proportion to the truncation wavenumber.

Table 1: The available time intervals and elapse times for 1-day simulation.

(a) AFES					
resolution	T159	T319	T639	T1279	T2559
Δt_{max}[s]	**400**	200	100	50	25
1 day simulation time[s]	8.02	27.9	184	1880	24900
(b) NICAM					
resolution	glevel-7	glevel-8	glevel-9	glevel-10	glevel-11
Δt_{max}[s]	**450**	225	113	57	29
1 day simulation time[s]	6.70	32.1	210	1520	12200

Thus guessed values are shown in Table 1.

From the data of maximum time interval and elapse time of one time step, the elapse times that are consumed for 1-day simulation can be estimated for each of models (the third line of each table).

4.3 Discussion

In general, the computational performance depends on the computer architecture, the degree of code optimization, and so on. It is difficult to give a conclusion by comparing two different numerical methods by the straightforward way. However, since both AFES and NICAM are well tuned to be performed on the Earth Simulator (see Shingu et al. (2002) for AFES and Goto et al. (2003) for NICAM), the comparison of those computational performances on the ES is appropriate to some degree.

One point at issue is the physical validity of short wave in the gridpoint model. Straightforwardly, two-grid scale structures are considered to be resolvable in the gridpoint model. In this sense, it is proper to compare the results of glevel-6 and T159, or glevel-7 and T319, and so on. Actually, we confirmed that there is only a little difference of physical results between glevel-6 and T159 in HSTC (Fig5). On the other hand, one regards a two-grid scale wave as a computational noise in the gridpoint model and argues that scales that have physical meanings are limited to four-grid scales in the gridpoint model (Pielke, 1991). In this case, the line with black rectangles in Fig.6(a) is shifted to the left line with black circles. Based on this consideration, it is proper to compare the glevel-7 and T159, or glevel-8 and T319, and so on.

Even if we employ the latter opinion, Table 1 shows a fact that the gridpoint method using a quasi-uniform grid system has computational advantage over the spectral transform method in the higher resolution than about T1000, resolvable scale of which corresponds to 40km. Thus, over this resolution the computational efficiency of the gridpoint model becomes superior to that of the spectral model with one order with regard to N. Besides, the overhead of communication between computational nodes is a severe problem in parallel computing for the spectral model, because the spectral transform method requires all-to-all communication. Fortunately, since the ES is designed to be able to do very fast data transfer (the ES has crossbar network with the data transfer rate of 24.6 GB/s bi-directionally between two nodes), this drawback is secondary in this study.

One remedy for the spectral model to reduce the computational cost may be the combination use of the linear grid system and the semi-Lagrangian advection scheme. There are two advantages in this framework; one is reduction of calculation associated with the transformation and the other is availability of long time interval over the CFL condition. However, for the former merit, the calculation is not reduced by the order but just by the factor 3/2. For the latter, if we choose too long time interval, the gravity wave that is an important wave in

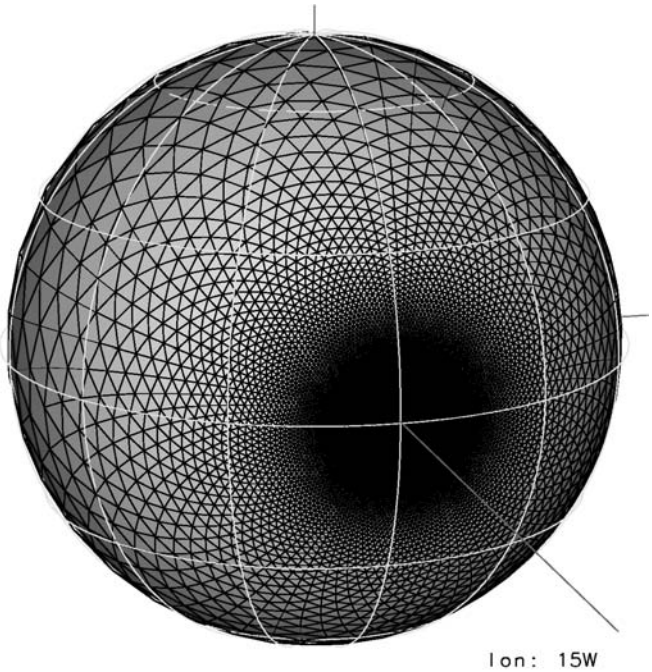

Figure 7: A stretched icosahedral grid by Schmidt transformation

the high resolution simulation is weakened by the implicit treatment.

5 Conclusion

In order to perform super-high resolution atmospheric simulations for the climate study, we developed a new dynamical core of nonhydrostatic global model. With the combination of the modified icosahedral grid (Tomita et al., 2001, 2002) and the conservative nonhydrostatic scheme (Satoh, 2002, 2003), we can make a high resolution AGCM that runs efficiently for climate simulations and is aimed to be used as a cloud-resolving AGCM in the near future.

The cloud microphysics holds a key to success of our modeling. Although many cloud microphysics schemes have been proposed up to date, the scheme that can be used anywhere (any latitude) in the globe has not yet been established. We should tune an existing scheme so as to be suitable to the entire globe or develop a new scheme by the method of trial and error. For an efficient inspection and/or development of cloud microphysics schemes by less computer resource, it is a good strategy to do so on a limited area (e.g., the tropical region, mid-latitude region, and so on) rather than the global area. A stretched grid by Schmidt transformation (Schmidt, 1977) (Fig.7) is useful for this purpose. We have just implemented several microphysics and are checking those performance on the stretched icosahedral grid. This technique can be also applied to a regional climate or forecast model.

References

Cullen, M. J. P., 1974. Integration of the primitive equations on a sphere using the finite element method. Quart. J. R. Met. Soc. 100, 555–562.

Cullen, M. J. P., Hall, C. D., 1979. Forecasting and general circulation results from finite element models. Quart. J. R. Met. Soc. 100, 571–592.

Goto, K., Tomita, H., Satoh, M., 2003. Computational performance of the dynamical part of a next generation climate model using an icosahedral grid on the earth simulator. In: Matsuno, K., Ecer, A., Periaux, J., Satofuka, N. (Eds.), Parallel Computational Fluid Dynamics 2002, New Frontiers and Multi-Disciplinary Applications. Elsevier, Ch. 2. Earth and Space Global Simulations and Earth Simulator, pp. 63–69.

Heikes, R. H., Randall, D. A., 1995a. Numerical Integration of the Shallow-Water Equations on a Twisted Icosahedral Grid. Part I : Basic Design and Results of Tests. Mon. Wea. Rev. 123, 1862–1880.

Heikes, R. H., Randall, D. A., 1995b. Numerical Integration of the Shallow-Water Equations on a Twisted Icosahedral Grid. Part II : A Detailed Description of the Grid and Analysis of Numerical Accuracy. Mon. Wea. Rev. 123, 1881–1887.

Held, I. M., Suarez, M. J., 1994. A proposal for the intercomparison of the dynamical cores of atmospheric general circulation models. Bull. Am. Meteorol. Soc. 73, 1825–1830.

Kasahara, A., 1974. Various vertical coordinate systems used for numerical weather prediction. Mon. Wea. Rev. 102, 509–522.

Majewski, D., Liermann, D., Prohl, P., Ritter, B., Buchhold, M., Hanisch, T., Paul, G., Wergen, W., 2002. The Operational Global Icosahedral-Hexagonal Gridpoint model GME: Description and High-Resolution Tests. Mon. Wea. Rev. 130, 319–338.

Masuda, Y., Ohnishi, H., Aug.4-8 1986. An integration scheme of the primitive equation model with an icosahedral-hexagonal grid system and its application to the shallow water equations. In: Short- and Medium-Range Numerical Weather Prediction. Collection of Papers Presented at the WMO/IUGG NWP Symposium, Tokyo. pp. 317–326.

Phillips, N. A., 1966. The Equations of Motion for a Shallow Rotating Atmosphere and the “Traditional Approximation”. J. Atmos. Sci. 23, 626–628.

Pielke, R. A., 1991. A reccomendated specific definition of resulution. Bull. Amer. Meteor. Soc. 72 (12), 1914–1914.

Ringler, T. D., Heikes, R. H., Randall, D. A., 2000. Modeling the atmospheric general circulation using a spherical geodesic grid: A new class of dynamical cores. Mon. Wea. Rev. 128, 2471–2490.

R.Laprise, 1992. The resolution of global spectral models. Bull. Amer. Meteor. Soc. 73 (9), 1453–1454.

Sadourny, R., Nov. 26-Dec. 4 1969. Numerical integration of the primitive equations on a spherical grid with hexagonal cells. In: Proceedings of the WMO/IUGG Symposium on Numerical Weather Prediction in Tokyo, Tech. Rep. of JMA. pp. VII45–VII52.

Sadourny, R., Arakawa, A., Mintz, Y., 1968. Integration of the nondivergent barotropic vorticity equation with an icosahedral hexagonal grid for the sphere. Mon. Wea. Rev. 96, 351–356.

Satoh, M., 2002. Conservative scheme for the compressible non-hydrostatic models with the horizontally explicit and vertically implicit time integration scheme. Mon. Wea. Rev. 130, 1227–1245.

Satoh, M., 2003. Conservative scheme for a compressible non-hydrostatic model with moist processes. Mon. Wea. Rev. 131, 1033–1050.

Schmidt, F., 1977. Variable fine mesh in spectral global model. Beitr. Phys. Atmos. 50, 211–217.

Shingu, S., Takahara, H., Fuchigami, H., Yamada, M., Tsuda, Y., Ohfuchi, W., Sasaki, Y., Kobayashi, K., Hagiwara, T., Habata, S., Yokokawa, M., Itoh, H., Otsuka, K., Nov.16-22 2002. A 26.58 tflops global atmospheric simulation with the spectral transform method on the earth simulator. In: the 2002 ACM/IEEE SC2002 Conference. pp. —, http://www.sc-2002.org/program(J(B*ech.html*.

Staniforth, A., Wood, N., 2003. The Deep-Atmosphere Euler Equations in a Generalized Vertical Coordinate. Mon. Wea. Rev. 131, 1931–1938.

Steppeler, J., Prohl, P., 1996. Application of finite volume methods to atmospheric models. Beitr. Phys. Atmosph. 69, 297–306.

Stuhne, G. R., Peltier, W. R., 1996. Vortex Erosion and Amalgamation in a New Model of Large Scale Flow on the Shere. J. Comput. Phys. 128, 58–81.

Stuhne, G. R., Peltier, W. R., 1999. New Icosahedral Grid-Point Discretizations of the Shallow Water Equations on the Sphere. J. Comput. Phys. 148, 23.

Tomita, H., Goto, K., Satoh, M., 2004. A comparison study of computational performace between a spectral transform model and a gridpoint model. In: Chetverushkin, B., Ecer, A., Periaux, J., Satofuka, N., Fox, P. (Eds.), Parallel Computational Fluid Dynamics, Advanced Numerical Methods, Software and Application. Elsevier, Ch. 6. Environmental and Ecology Problems, pp. 333–340.

Tomita, H., Satoh, M., 2004. A new dynamical framework of nonhydrostatic global model using the icosahedral grid. Fluid Dyn. Res. 34, 357–400.

Tomita, H., Satoh, M., Goto, K., 2002. An Optimization of the Icosahedral Grid Modified by Spring Dynamics. J. Comput. Phys. 183, 307–331.

Tomita, H., Tsugawa, M., Satoh, M., Goto, K., 2001. Shallow Water Model on a Modified Icosahedral Geodesic Grid by Using Spring Dynamics. J. Comput. Phys. 174, 579–613.

Wicker, L. J., Skamarock, W. C., 1998. Time-splitting scheme for the elastic equations incorporating second-order Runge-Kutta time differencing. Mon. Wea. Rev. 126, 1992–1999.

Wicker, L. J., Skamarock, W. C., 2002. Time-splitting methods for elastic models using forward time schemes. Mon. Wea. Rev. 130, 2088–2097.

Williamson, D. L., 1968. Integration of the barotropic vorticity equation on a spherical geodesic grid. Tellus 20, 642–653.

Williamson, D. L., 1969. Integration of the primitive barotropic model over a spherical geodesic grid. Mon. Wea. Rev. 98, 512–520.

Williamson, D. L., Drake, J. B., Hack, J. J., Jacob, R., Swarztrauber, P. N., 1992. A Standard Test Set for Numerical Approximations to the Shallow Water Equations in Spherical Geometry. J. Comput. Phys. 102, 211–224.